Internal Report
DESY FH1K–96–01
May 1996

The Structure Function $F_2(x, Q^2)$ at Low Q^2 from Radiative Events with H1 at HERA

by

L. Favart, M. Fleischer, M. Hütte, Z. Zhang

Internal Report
DESY FH1K-96-01
May 1996

The Structure Function $F_2(x, Q^2)$ at Low Q^2 from Radiative Events with H1 at HERA

L. FAVART[1], M. FLEISCHER[2], M. HÜTTE[2], AND Z. ZHANG[1]

[1] Laboratoire de L'Accélérateur Linéaire, IN2P3-CNRS et
Université de Paris-Sud, Orsay, France
[2] Institut für Physik, Universität Dortmund, Germany

Abstract

Using the 1994 data collected with the H1 detector, the proton structure function $F_2(x, Q^2)$ has been measured for Q^2 values down to $1.5\,\mathrm{GeV}^2$ and $x > 10^{-4}$ using deep inelastic radiative events with hard photon emission collinear with the incident electron. The accessible kinematic domain is lower in Q^2 than for non-radiative events because the center of mass energy is reduced. The results are compared with other measurements, model predictions, and a QCD extrapolation to the low Q^2 values of other independent structure function measurements based on non-radiative events.

1 Introduction

Radiative corrections are known to be large in certain regions of the HERA kinematic domain due to hard photon emission. These corrections are somewhat uncertain because of our ignorance of the proton structure function $F_2(x, Q^2)$ for values of Q^2 below those currently accessible at HERA by both H1 and ZEUS, where x is the Bjorken variable that can be interpreted in the quark parton model as the fraction of proton momentum carried by the struck parton and Q^2 is the momentum transfer squared carried by the exchanged virtual photon. The measurement of the cross section of these radiative events allows a direct control of this uncertainty.

It will be very interesting to see below which critical Q_0^2 values the (perturbative) QCD prediction for the behaviour of the structure functions starts to fail. Measurements from low energy hadron-hadron experiments and high energy HERA experiments show that the cross section for photoproduction (γp) processes (at $Q^2 \simeq 0\,\mathrm{GeV}^2$) has only a weak dependence on energy, whereas the structure function $F_2(x, Q^2)$ as well as the cross section for deep inelastic scattering (DIS) in the HERA kinematic domain at Q^2 larger than a few GeV^2 has a rather steep rise as x decreases. This provides further motivation to study the intermediate Q^2 region to understand the dynamics of the transition region between the two regimes.

In this paper, we show that lower Q^2 can be reached using DIS events from the radiative process $ep \to e\gamma X$ with hard photon emission collinear to the incident electron[1] beam. The accessible kinematic domain is lower in Q^2 than for non-radiative DIS events because radiative events can be interpreted as non-radiative events with reduced electron beam energy and therefore reduced center of mass energy [1].

First experimental studies of this process using H1 1992 data can be found in [2] and recent results with 1993 data can be found in [3, 4, 5]. A tenfold increase of the integrated luminosity ($\int \mathcal{L} = 2.7\,\mathrm{pb}^{-1}$) in 1994 has made possible for the first time a measurement of the proton structure function $F_2(x, Q^2)$ for Q^2 values down to 1.5 GeV^2 [6]. A similar measurement has been published recently by the ZEUS collaboration [7].

The paper is organized as follows. After a short description of the H1 detector in section 2, the event selection, the background estimation, and the Monte Carlo (MC) simulation are shown in section 3. The reconstruction of kinematic variables and the definition of the bin size for the analysis is outlined in section 4. In section 5 detailed comparisons between data and MC events are shown together with the determination of various efficiencies. The analysis method and the results are presented in section 6 followed by the conclusion in section 7.

[1] HERA ran in 1994 with 27.5 GeV electrons/positrons and 820 GeV protons. For simplicity, in the following *electrons* refer to both electrons and positrons.

2 H1 detector

The H1 detector is described in detail in [8]. Here only those subdetectors which are of importance for this analysis are briefly introduced (Fig. 1).

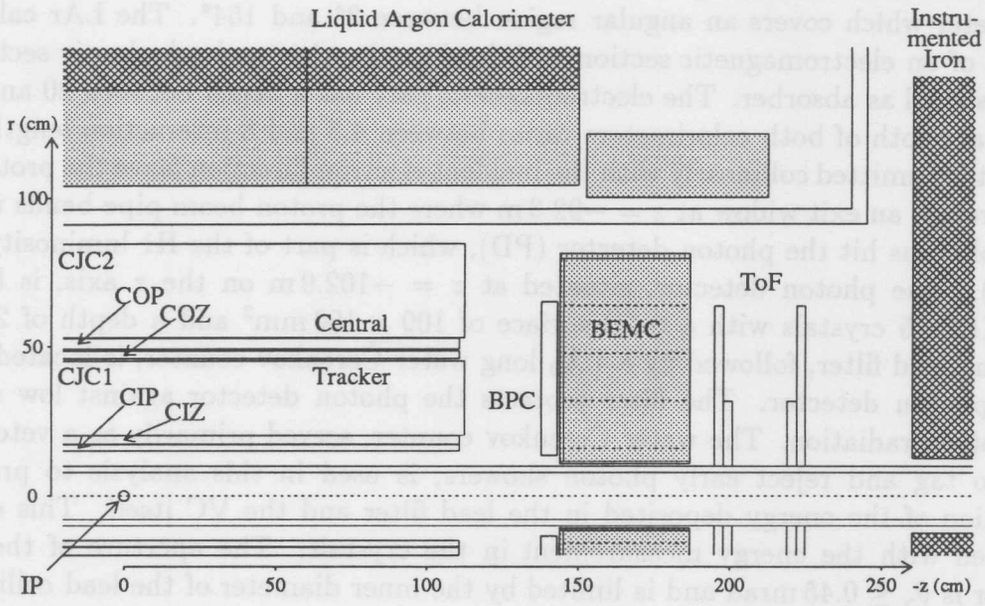

Figure 1: *A schematic view of the backward H1 detector.*

The scattered electrons studied in this paper are detected with the backward electromagnetic calorimeter (BEMC) [9]. The BEMC is made of 88 lead/scintillator stacks with a size of $16 \times 16\,\mathrm{cm}^2$ and a depth of 21.7 radiation lengths (X_0) corresponding to about one interaction length. The four inner stacks around the beampipe are of triangle shape. The angular[2] coverage of the BEMC is $151° < \theta < 176°$; its electromagnetic energy resolution is $\sigma_E/E = 0.39/E \oplus 0.10/\sqrt{E} \oplus 0.017$. A four plane multiwire proportional chamber (BPC) is located in front of the BEMC at $z = -141.2\,\mathrm{cm}$. The BPC angular acceptance is $155° < \theta < 174°$ with a spatial resolution of about 1.5 mm in the transverse plane. The scattered electron polar angle θ_e is determined from the positions of the BPC hit and of the interaction vertex.

A scintillator hodoscope (TOF) situated behind the BEMC is used to veto proton-induced background events based on their early time of arrival compared with nominal *ep* collisions.

The vertex positions are reconstructed from charged particles detected both from the central jet chamber (CJC) and from the forward tracker (FT). Tracks crossing the CJC are measured with a transverse momentum resolution of $\delta p_T/p_T < 0.01 p_T/\mathrm{GeV}$. The CJC, 2.2 m long, is supplemented by two cylindrical drift chambers (CIZ/COZ) at radii

[2]The polar angle θ is defined with respect to the proton beam direction($+z$)

of 18 and 47 cm, respectively, to determine the z coordinate of the tracks. To each of the z drift chambers a cylindrical proportional chamber (CIP/COP) is attached for triggering purposes. The FT is made of three identical modules measuring charged particles emitted in the forward direction (7° to 20°).

Hadronic final state energies are measured in the highly segmented liquid argon (LAr) calorimeter which covers an angular region between 3° and 154°. The LAr calorimeter consists of an electromagnetic section with lead as absorber and a hadronic section with stainless steel as absorber. The electromagnetic part has a depth between 20 and 30 X_0. The total depth of both calorimeters varies between 4.5 and 8 interaction lengths.

Photons emitted collinearly with the incident electron direction leave the proton beam pipe through an exit widow at $z = -92.3\,\mathrm{m}$ where the proton beam pipe bends upwards. These photons hit the photon detector (PD), which is part of the H1 luminosity system (Fig. 2). The photon detector, situated at $z = -102.9\,\mathrm{m}$ on the z axis, is built out of 25 KRS-15 crystals with a total surface of $100 \times 100\,\mathrm{mm}^2$ and a depth of $22\,X_0$. A $2\,X_0$ long lead filter, followed by a $1\,X_0$ long water Čerenkov counter, is located in front of the photon detector. The filter protects the photon detector against low energetic synchrotron radiation. The water Čerenkov counter, served primarily as a veto counter (VC) to tag and reject early photon showers, is used in this analysis to provide an estimation of the energy deposited in the lead filter and the VC itself. This energy is combined with the energy measurement in the crystals. The aperture of the photon detector is $\theta_\gamma \leq 0.45\,\mathrm{mrad}$ and is limited by the inner diameter of the lead collimator in front of it.

Another part of the H1 luminosity system is the electron tagger (ET) which is located beside the electron beam pipe at $z = -33.4\,\mathrm{m}$. It is made of 49 crystals (of the same type as the photon detector calorimeter), covering a total area of $154 \times 154\,\mathrm{mm}^2$. It is used in this analysis to detect background events with small angle scattered electrons.

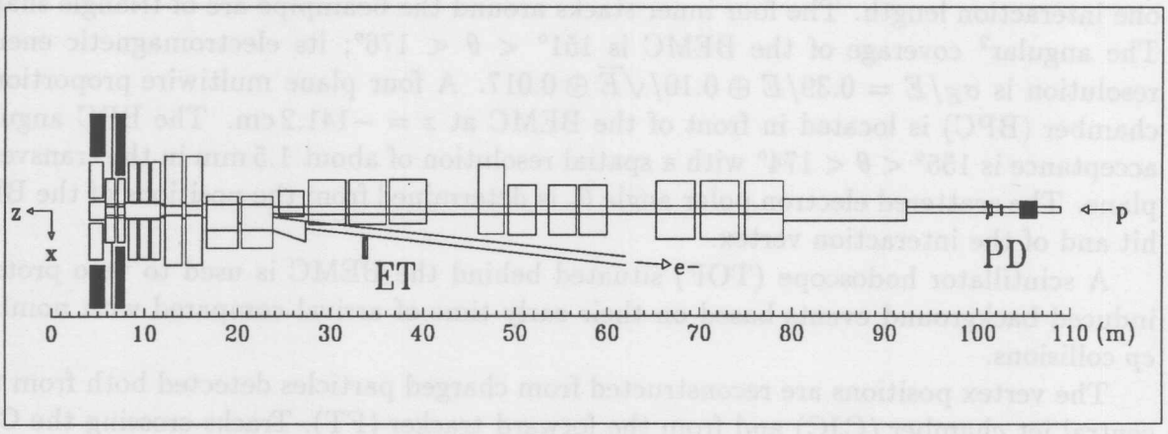

Figure 2: *A schematic view of the H1 luminosity system.*

3 Event selection and Monte Carlo simulation

3.1 Event selection

The selection of DIS events with hard photon emission collinear to the incident electron is based on the following requirements:

- The scattered electron, which is defined to be the most energetic cluster in the BEMC, has to satisfy:

$$\begin{aligned} \text{Energy}: &\quad E'_e > 8\,\text{GeV} \\ \text{Cluster radius}: &\quad RCLU < 5\,\text{cm} \\ \text{Distance between BPC hit/cluster center}: &\quad DBPC < 4\,\text{cm} \\ \text{Fiducial cuts on BPC hit}: &\quad \begin{cases} \sqrt{x^2_{\text{BPC}} + y^2_{\text{BPC}}} > 15\,\text{cm} \\ |x_{\text{BPC}}| + |y_{\text{BPC}}| > 18\,\text{cm} \end{cases} \\ \text{The presence of a BEMC trigger signal}: &\quad s_0 = 1 \end{aligned} \tag{1}$$

  where the subtrigger bit s_0 is set if a BEMC cluster has a triggered energy larger than 7 GeV plus additional information from the TOF. An electron candidate so defined has a misidentification probability of $\sim$ 3% when calculated using MC simulation.

- An energetic photon detected in the photon detector is required to have:

$$E_\gamma = E_{\text{PD}} + E_{\text{VC}} > 4\,\text{GeV} \tag{2}$$

  where E_{PD} and E_{VC} are the energies deposited in the photon detector and in the water Čerenkov counter. This condition removes beam related background events and cosmic rays which produce energetic showers in the BEMC.

- There must be a vertex with coordinate z_{vtx} to be reconstructed within ± 35 cm of the average vertex position z_o:

$$|z_{\text{vtx}} - z_o| < 35\,\text{cm} \tag{3}$$

  The spread in z_{vtx} is about 3 times the vertex resolution σ_{vtx} in the interaction region (Fig. 11). Since the vertex position is needed for defining the polar angle θ_e of the scattered electron in the backward direction (BPC/BEMC), this requirement helps to reduce the kinematic reconstruction uncertainty. Furthermore, it efficiently suppresses the beam related background events.

- It turns out that the main source of background is due to pile-up events due to accidental coincidence of DIS and γp events with a Bethe-Heitler [10] (BH)

Bremsstrahlung event ($ep \rightarrow e\gamma p$) in a time window of ± 5 ns. These pile-up events are efficiently rejected with the following cuts:

$$E_{\mathrm{etag}} < 2\,\mathrm{GeV}$$
$$\Delta < 0.5 \quad \text{where} \quad \Delta = \frac{E_\gamma - E_{\mathrm{miss}}}{E_\gamma} \tag{4}$$

where E_{etag} is the energy deposited in the electron tagger. The quantity Δ compares the measured photon energy in the photon detector E_γ with the expected missing energy E_{miss}:

$$E_{\mathrm{miss}} = E_e^0(y_e - y_{\mathrm{JB}}) \tag{5}$$

with

$$y_e = 1 - \frac{E'_e}{E_e^0}\sin^2\frac{\theta_e}{2} = \frac{1}{2E_e^0}\left[2E_e^0 - (E'_e - p'_{z,e})\right]$$
$$y_{\mathrm{JB}} = \frac{\Sigma_h}{2E_e^0} = \frac{\sum_i (E_i - p_{z,i})}{2E_e^0} \tag{6}$$

where E_e^0 is the electron beam energy, y_e and y_{JB} [11] are inelasticity parameters measured respectively from the scattered electron and all hadronic final state particles detected in the main H1 detector (without including the luminosity system). One thus expects for radiative DIS events $\Delta = 0$ ($E_\gamma = E_{\mathrm{miss}}$) while for pile-up DIS+BH events $\Delta = 1$ ($E_{\mathrm{miss}} = 0$). More details concerning these cuts and the remaining background events are discussed in the next section.

In order to minimize the influence of occasional failure of some subdetector components there are several additional requirements for inclusion of data:

- Events are selected only from good and medium quality runs which are in trigger phases 3 and 4 and where most of the important subdetectors are turned on and the background rate is relatively small.
- The following subdetectors TOF, CJC, BEMC, BPC, LAr, the electron tagger and the photon detector have their high voltages switched on for more than 70% of the time.
- The BEMC subtrigger bit s_0 must be enabled without any prescaling.

3.2 Background studies

After applying the selection cuts described in the previous section, a sample of 8229 events has been selected. It consists mainly of the following types of events[3]:

[3]Note that the acceptance for photons from radiative DIS events is about 30% while for BH events it is about 98% due to the different angular distributions of photon emission.

1. Radiative DIS events alone or in random coincidence with BH events (with the probability to be discussed below) where the radiated photon is detected in the PD,

2. Pile-up events due to radiative DIS with BH events where the radiated photon from the DIS event is not detected,

3. Pile-up events due to non-radiative DIS with BH events,

4. Pile-up events due to γp with BH events or inelastic BH events alone.

Events of type 1 constitute the signal since the radiated photons are collinear with respect to the direction of the incident electron. All other events are background. For the events of type 4, the backward clusters are wrongly identified as electrons. This is due to the fact that the BEMC has only one interaction length and showers produced by hadronic incidence cannot be absorbed completely. Therefore an unambiguous separation between electrons and hadrons is not possible at low energies.

The probability for random coincidence depends on the minimum photon energy ($E_\gamma^{\min}$) of BH events. According to an analysis of BH events [12], this probability is 5.6% for $E_\gamma^{\min} = 0.13\,\mathrm{GeV}$, which is consistent with the value determined using the Δ distribution described below.

As mentioned in sec. 3.1 the variable Δ can be used to reject pile-up events. The distribution of Δ is shown in Fig. 3 for six different event samples. The plots on the left show those events which have activity in the electron tagger ($E_{\mathrm{etag}} > 2\,\mathrm{GeV}$, tagged sample) while the plots on the right correspond to the non-tagged sample. The dependence on E'_e is shown in three different energy ranges indicated with the axis on the right side. As expected, the peaks around one in the two upper plots are due to DIS+BH events. The normalization of this background is fixed[4] by the upper left plot and confirmed with the upper right one for events at high Δ values ($\Delta > 0.8$) where the expected signal (peaking around $\Delta = 0$) does not contribute. The difference (4%) is taken as the uncertainty in the background subtraction of pile-up events of types 2 and 3.

The normalization for the events of type 4 is fixed by the lower left plot after the DIS+BH events have been subtracted. In this way, any possible background contribution from inelastic BH events (with photons being detected in the PD) is also taken into account. In fact, among the estimated background events of type 4, only about one third is expected from γp events in random coincidence with BH events using the probability given above. A 30% uncertainty is assigned for this normalization due to the missing inelastic BH process in MC and to the dependence on the low energy spectrum of the structure function.

The relative contribution of these background events after all selection cuts is smaller than 10% in most of the (x, Q^2) bins to be defined below and does not exceed 30% for bins at high y.

[4]With this method we found a probability for random coincidence of 6.4% for $E_\gamma^{\min} = 0.1\,\mathrm{GeV}$, which corresponds to 6.0% for $E_\gamma^{\min} = 0.13\,\mathrm{GeV}$, and is consistent with the value mentioned above. The large value of this method may be understood since second order overlaps are included.

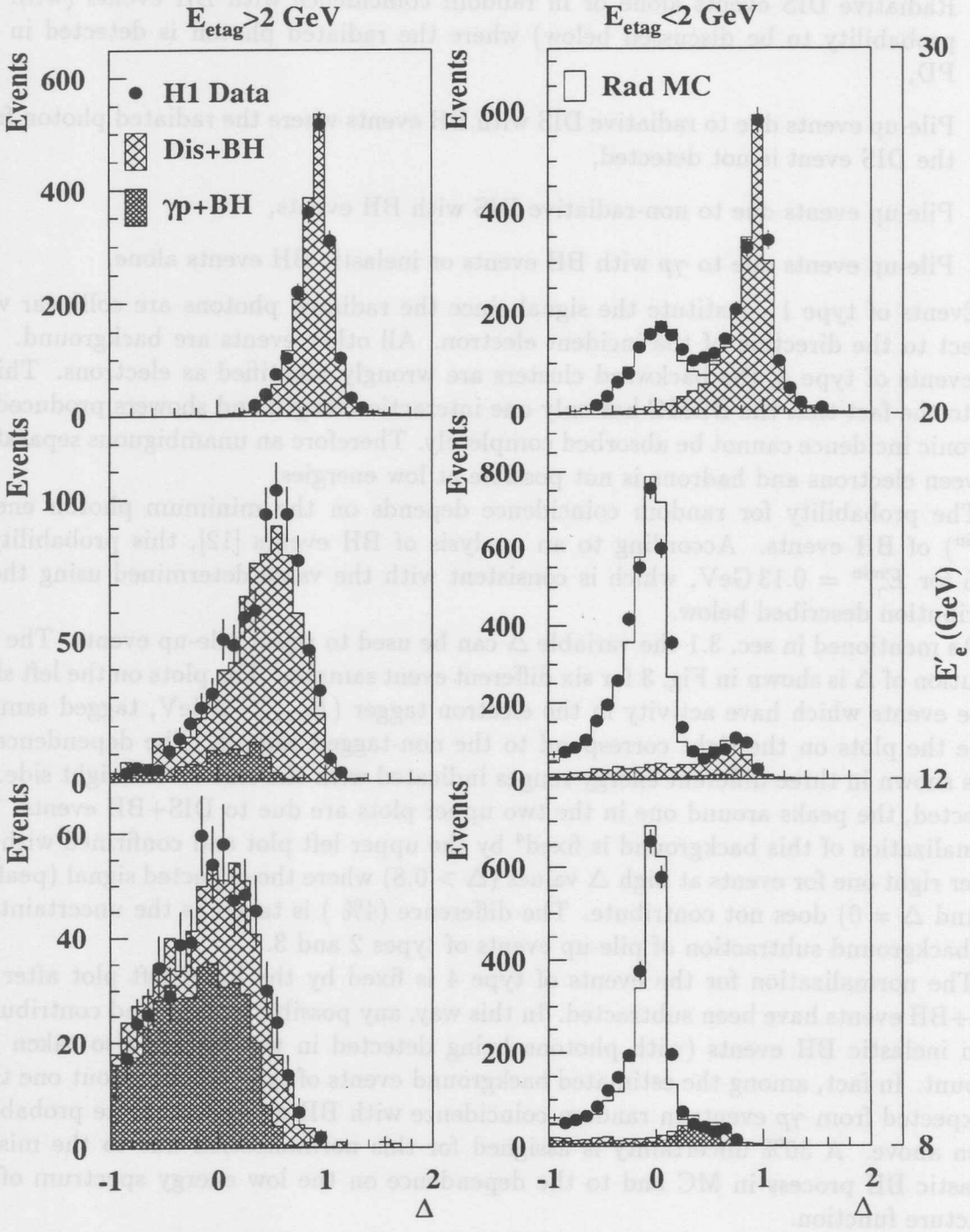

Figure 3: *Distribution of Δ (see text for definition) for tagged events (left plots) and for non-tagged events (right ones) in three different electron energy ranges as shown with the axis on the right side.*

3.3 Monte Carlo simulation

Monte Carlo event simulation is used to correct for detector acceptance and smearing effects. The detector simulation is based on the GEANT program [13] and incorporates our understanding of the detector and test beam results. Neutral current DIS events (both radiative events and non-radiative events) are generated using DJANGO [14], which is based on HERACLES [15] for the electroweak interaction and on LEPTO [16] for simulating the hadronic final state. HERACLES includes the complete first order electroweak radiative corrections, real Bremsstrahlung photons and the longitudinal structure function. LEPTO uses the colour-dipole model as implemented in ARIADNE [17] for the QCD cascade and JETSET [18] is used for the hadronisation. The GRV [19] parton density parametrization was used for the generation of events because this parametrization provided an adequate description of previous H1 and ZEUS measurements [20, 21] and is the only QCD prediction that starts at a Q_0^2 below $1.0\,\mathrm{GeV}^2$.

The γp events were simulated using the PHOJET generator [22], which generates the total γp cross section by taking into account both soft and hard processes.

The BH events were generated according to the Bethe-Heitler approximation [10] in which the proton recoil energy is neglected, i.e. $E'_e + E_\gamma \simeq E^0_e$. The acceptance of the electron tagger was determined directly from the H1 data.

After the event simulation, the MC events were subjected to the same reconstruction and analysis chain as the real data.

4 Kinematics reconstruction and bin definition

4.1 Kinematics reconstruction

Because of the hermetic nature of the H1 experiment, it is possible to use different methods for reconstructing the kinematics. Shown in the following are three examples of these methods based either on the scattered electron alone or on all available information from both electron and hadronic final state particles:

- Electron method (E):

$$\begin{aligned} Q^2_e &= 4E^{\text{eff}}_e E'_e \cos^2\frac{\theta_e}{2} \\ y_e &= 1 - \frac{E'_e}{E^{\text{eff}}_e}\sin^2\frac{\theta_e}{2} \\ x_e &= \frac{Q^2_e}{y_e s^{\text{eff}}} \end{aligned} \tag{7}$$

with

$$s^{\text{eff}} = 4E^{\text{eff}}_e E^0_p \tag{8}$$

where $E^{\text{eff}}_e \equiv E^0_e - E_\gamma$ is the effective (reduced) beam energy assuming collinearity of initial state radiation, and E^0_e, E_γ, E'_e, θ_e, and E^0_p are respectively the electron beam energy, the radiative photon energy, the scattered electron energy and angle, and the proton beam energy.

- Sigma method [23] (Σ):

$$\begin{aligned} y_\Sigma &= \frac{\Sigma_h}{\Sigma_h + E'_e(1-\cos\theta_e)} \\ Q^2_\Sigma &= \frac{E'^2_e \sin^2\theta_e}{1-y_\Sigma} \\ x_\Sigma &= \frac{Q^2_\Sigma}{y_\Sigma s^{\text{eff}}} \end{aligned} \tag{9}$$

where Σ_h is defined in eq. (6). Since this method relies mostly on the hadronic measurement, it has small radiative corrections.

- Double angle method [24] (DA):

$$\begin{aligned} Q^2_{DA} &= 4E^{\text{eff}\,2}_e \frac{\cot(\theta_e/2)}{\tan(\theta_e/2)+\tan(\theta_h/2)} \\ y_{DA} &= \frac{\tan(\theta_h/2)}{\tan(\theta_e/2)+\tan(\theta_h/2)} \\ x_{DA} &= \frac{Q^2_{DA}}{y_{DA} s^{\text{eff}}} \end{aligned} \tag{10}$$

with

$$\tan(\theta_h/2) = \frac{\Sigma_h}{p_T^h} \tag{11}$$

where p_T^h is the total transverse momentum of all hadronic final state particles.

The definitions are the same as for the non-radiative events except here we are using the effective electron beam energy E_e^{eff} instead of E_e^0.

The resolution on Q^2 and x for these three methods is compared and shown in Fig. 4 for different ranges of the inelasticity y. It is clear from this comparison that the E and the Σ methods are superior to the DA method in the low Q^2 region considered and will be employed in this analysis for cross-checking the results. The E method has the best resolution on Q^2 in all y ranges and the best resolution on x in the high y range while the Σ method has a better resolution on x for y values below 0.15.

4.2 Bin definition

The size of bins in x and Q^2 is taken to be as small as in commensurate with the available statistics and the effects of bin-to-bin migration of events due to the finite resolution in x and Q^2. The bin centres (edges) defined for this analysis are shown in Table 1.

6 bins in Q^2							
Bin edges in $\log Q^2(\text{GeV}^2)$	0	0.25	0.5	0.625	0.75	0.875	1
Bin center in $Q^2(\text{GeV}^2)$		1.5	2.5	3.5	5	6.5	8.5
5 to 3 bins in x depending on Q^2							
Bin edges in $\log(x)$	-4.2	-3.8	-3.4	-3	-2.6	-2.2	
Bin center in x	0.0001	0.00025	0.00063	0.00158	0.00398		

Table 1: *The bin definition in Q^2 and x for the analysis.*

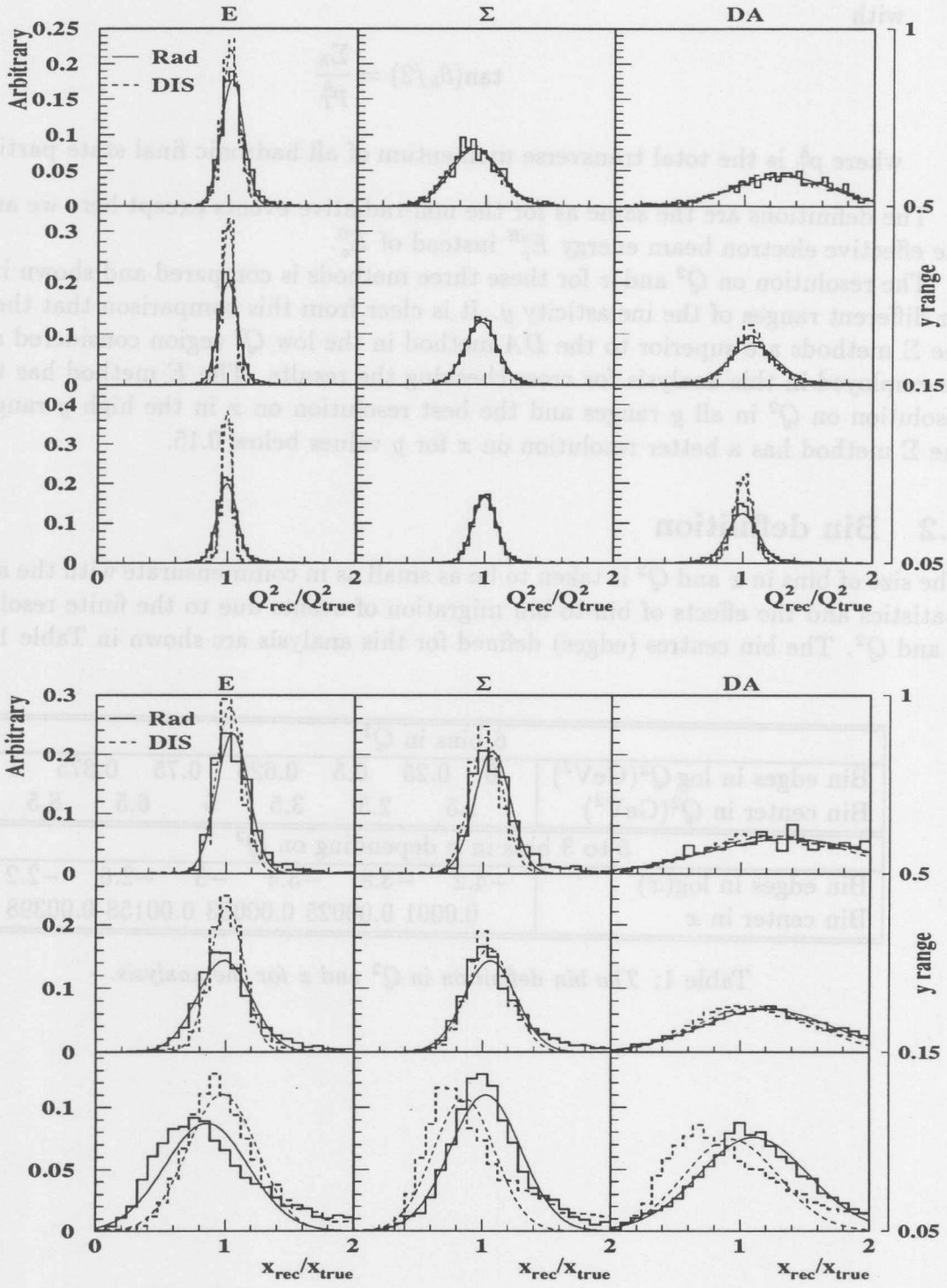

Figure 4: *A comparison of the resolution in Q^2(upper plot) and in x (lower plot) reconstructed with three different kinematic methods: the electron method (E, left column), the sigma method (Σ), and the double angle method (DA, right column) for radiative DIS events (Rad, solid lines) and for non-radiative DIS events(dashed lines). To guide the eye gaussian fits to the corresponding histograms are also shown.*

5 Efficiency and Comparison between data and MC simulation

In this section we describe the quantitative comparison made between real and simulated events. Before this could be done it is necessary to ensure that the efficiencies of the selection cuts (1)–(4) were well reproduced by the MC simulation. For those efficiencies which were not well reproduced in the MC, additional corrections had to be made.

5.1 Trigger efficiency

The event sample was required to be triggered by the BEMC trigger. The efficiency of this trigger was determined as function of the electron energy and the impact position with an independent event sample (dominated by non-radiative events) which were triggered with an independent tracker-related trigger. The trigger efficiency was also simulated in the MC, but here we prefered to correct it only on the data side keeping the full statistics from the MC.

During the 1994 data taking period the four inner triangle stacks in the BEMC did not contribute to the trigger for most of the time ("closed triangle" period). During the last weeks of data taking these modules were included in the trigger ("open triangle" period). It turned out that for the open triangle period the trigger efficiency did not depend on the impact position but on the electron energy only. For electrons with an energy of 8 GeV an efficiency of $\simeq 80\%$ was found and from 11 GeV on it was found to be $\simeq 100\%$.

For the closed triangle period the trigger efficiency strongly depends on the impact position, as can be seen in Fig. 5. To ensure the trigger efficiency to be acceptably high an additional cut, $\max\{|x_{\mathrm{BPC}}|, |y_{\mathrm{BPC}}|\} > 13.5\,\mathrm{cm}$, was applied for this period, as it is indicated in Fig. 5. In the region $\max\{|x_{\mathrm{BPC}}|, |y_{\mathrm{BPC}}|\} > 17\,\mathrm{cm}$ the trigger efficiency depended on the electron energy only, while in the region $13.5\,\mathrm{cm} < \max\{|x_{\mathrm{BPC}}|, |y_{\mathrm{BPC}}|\} < 17\,\mathrm{cm}$ it was determined as function of the electron energy E'_e and $\max\{|x_{\mathrm{BPC}}|, |y_{\mathrm{BPC}}|\}$. The result is shown in Fig. 6.

In Fig. 7 the average trigger efficiency for each (x, Q^2) bin is shown for the E and the Σ method, separately for the open triangle and the closed triangle periods. The efficiency is above 80% for all considered bins. As expected it is higher for the open triangle period.

5.2 Vertex efficiency

The vertex inefficiency has two contributions: either there is no reconstructed vertex or there is a vertex but outside of the cut in eq. (3). For radiative DIS events, due to the hard photon radiation and thus reduced center of mass energy, hadronic final state particles formed from the struck parton have lower transverse momentum with respect to the incident proton direction than those in non-radiative DIS events, and therefore the probability of having a reconstructed vertex is significantly reduced.

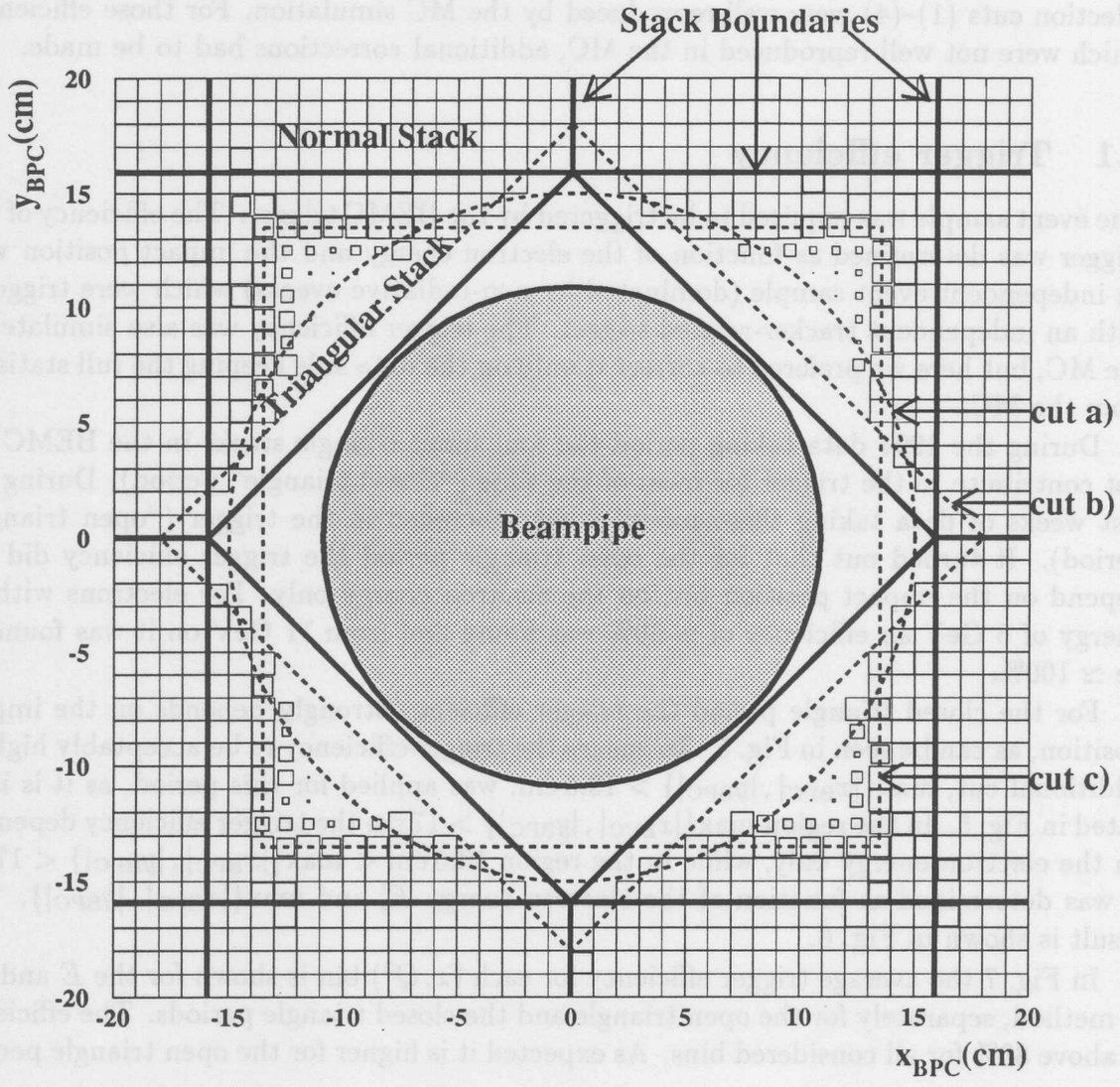

Figure 5: *Trigger efficiency in the BEMC inner region as function of the impact position* $(x_{\mathrm{BPC}}, y_{\mathrm{BPC}})$ *for the closed triangle period. The efficiency is proportional to the box size with the full box size corresponding to 100%. The electron energy was required to be far above the trigger threshold to separate the spatial dependence of the trigger efficiency from the energy dependence. The cuts a) and b) are always applied, see eq. (1). The cut c)* $\max\{|x_{\mathrm{BPC}}|, |y_{\mathrm{BPC}}|\} > 13.5\,\mathrm{cm}$ *was applied for the closed triangle period only to ensure a high trigger efficiency.*

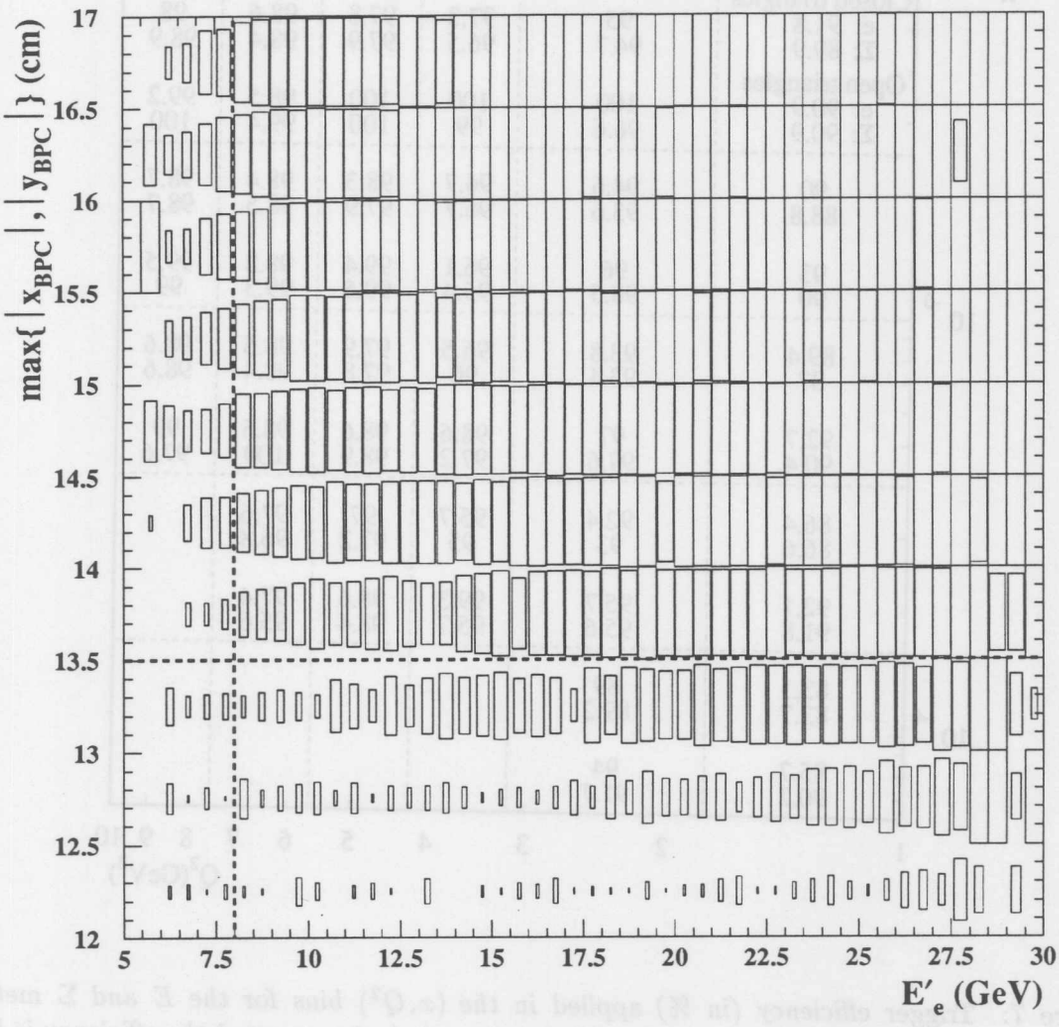

Figure 6: *Trigger efficiency in the BEMC inner region as function of E'_e and* $\max\{|x_{\mathrm{BPC}}|, |y_{\mathrm{BPC}}|\}$ *for the closed triangle period. As in Fig. 5, the efficiency is proportional to the box size with the full box size corresponding to 100%. The selection cuts are indicated by dashed lines.*

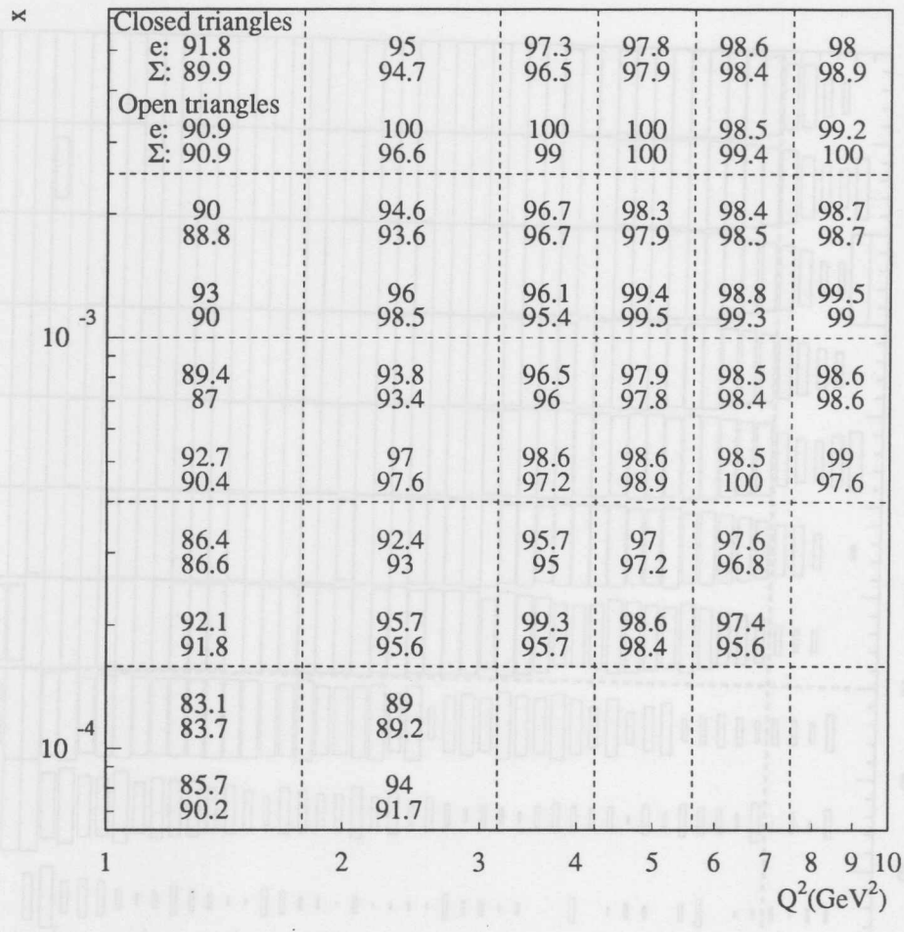

Figure 7: *Trigger efficiency (in %) applied in the (x, Q^2) bins for the E and Σ methods, separately for the open triangle and closed triangle period. As expected the efficiency is higher during the open triangle period, when the inner triangle stacks of the BEMC were included in the trigger readout.*

The efficiencies may be determined for radiative MC events in the following way:

$$\epsilon_{\exists\, z_{\rm vtx}} = \frac{N(\text{all cuts except } |z_{\rm vtx} - z_o| < 35\,\text{cm})}{N(\text{all cuts except } \exists\, z_{\rm vtx} \text{ and } |z_{\rm vtx} - z_o| < 35\,\text{cm})} = 82.6 \pm 0.3\% \qquad (12)$$

and

$$\epsilon_{|z_{\rm vtx} - z_o| < 35\,\text{cm}} = \frac{N(\text{all cuts})}{N(\text{all cuts except } |z_{\rm vtx} - z_o| < 35\,\text{cm})} = 94.4 \pm 0.2\% \qquad (13)$$

Unfortunately this simple method cannot be applied to the real data because the efficiency may be biased by the residual background events contained in the denominators. Therefore another method has to be used.

We have used the CIP method [25], which defines in the rz plane the crossing point with the z axis of a straight line formed with a BPC point and a coincident CIP point as a vertex position $z_{\rm CIP}$ independent of the fact whether $z_{\rm vtx}$ is available or not (see Fig. 1). If $z_{\rm vtx}$ does exist, we have checked that the appropriate correlation is seen both in data and in MC (Fig. 8).

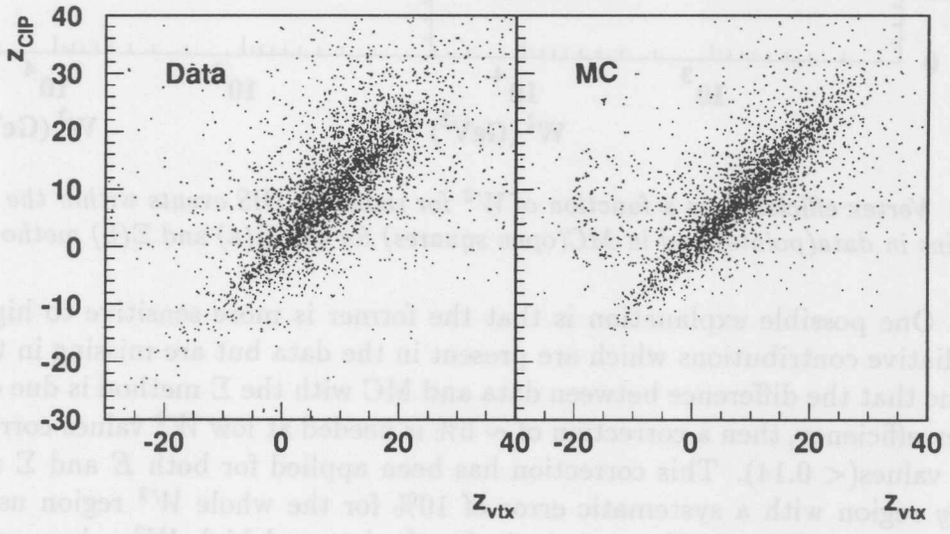

Figure 8: *Correlation between $z_{\rm vtx}$ and $z_{\rm CIP}$ in data (left) and MC (right).*

By applying the cut in eq. (3) using $z_{\rm CIP}$, namely:

$$|z_{\rm CIP} - z_o| < 35\,\text{cm}\,, \qquad (14)$$

to both the numerators and the denominators in eqs.(12) and (13), the vertex inefficiencies are determined both for data and for MC:

Data :	$\epsilon_{\exists\, z_{\rm vtx}} = 82.8 \pm 0.5\%$	(15)
	$\epsilon_{\|z_{\rm vtx} - z_o\| < 35\,\text{cm}} = 94.2 \pm 0.4\%$	
MC :	$\epsilon_{\exists\, z_{\rm vtx}} = 83.8 \pm 0.4\%$	
	$\epsilon_{\|z_{\rm vtx} - z_o\| < 35\,\text{cm}} = 95.2 \pm 0.2\%$	

Therefore the comparison between data and MC is satisfactory for the total samples of events, in which events at relatively high Q^2 values dominate due to the bias introduced by the limited CIP geometrical acceptance. Selecting events only at the considered (x, Q^2) region as defined in sec. 4.2, a difference shows up between data and MC when the efficiencies are plotted as a function of the hadronic invariant mass squared (W^2)[5] in Fig. 9. The difference is more pronounced using the E method than using the Σ

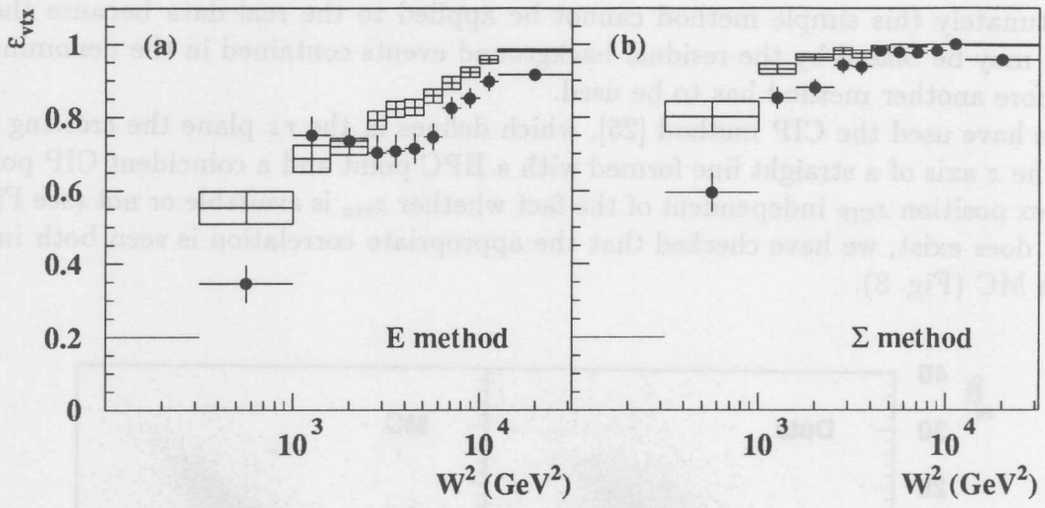

Figure 9: *Vertex efficiency as a function of W^2 for radiative DIS events within the considered (x, Q^2) bins in data(points) and in MC(open squares) for the E(a) and Σ(b) methods.*

method. One possible explanation is that the former is more sensitive to higher order QED radiative contributions which are present in the data but are missing in the MC. If we assume that the difference between data and MC with the Σ method is due entirely to the vertex efficiency, then a correction of $\sim 6\%$ is needed at low W^2 values corresponding to low y values(< 0.14). This correction has been applied for both E and Σ method in the low y region with a systematic error of 10% for the whole W^2 region using the E method, and of 10% and 4% respectively for the low and high W^2 values using the Σ method.

5.3 BPC efficiency

As for the vertex efficiency calculation, the BPC efficiency may be determined for MC from the appropriate ratio, namely:

$$\epsilon_{\mathrm{BPC}} = \frac{N(\text{all cuts})}{N(\text{all cuts except } DBPC < 4.0\,\mathrm{cm})} = 95.9 \pm 0.1\% \qquad (16)$$

[5]We have chosen W^2 since the vertex efficiency is closely related to the activity measured in the detector from the hadronic final state particles.

However this simple method cannot be applied to the data since the remaining photoproduction background events will bias the efficiency determination. This background may be partly identified [26] by checking whether there is an expected hit in the CIP in the road formed with the vertex position and the center of gravity of the BEMC cluster. Adding this requirement both to the numerator and to the denominator of eq. (16), one gets the following efficiencies for data and MC:

$$\boxed{\begin{array}{ll} \text{Data :} & \epsilon_{\text{BPC}} = 97.8 \pm 0.2\% \\ \text{MC :} & \epsilon_{\text{BPC}} = 98.4 \pm 0.1\% \end{array}} \tag{17}$$

The BPC efficiency in data thus agrees with the MC. The difference seen between two MC values may be attributed to the fact that the former includes the electron misidentification probability (sec. 3.1).

5.4 Photon energy calibration

For a precise measurement of the energy of the radiated photon it is important to know the energy calibration [12] of the photon detector with high precision. The off-line calibration of the photon detector (and also of the electron tagger) has been determined with a sample of BH events. These events were selected using the following requirements:

$$\begin{aligned} & E_{\text{ET}} \geq 4\,\text{GeV} \\ & E_\gamma \geq 4\,\text{GeV} \\ & 24\,\text{GeV} \leq E_{\text{ET}} + E_\gamma \leq 31\,\text{GeV} \\ & |x_{\text{ET}}| \leq 65\,\text{mm} \quad \text{and} \quad |y_{\text{ET}}| \leq 65\,\text{mm} \end{aligned} \tag{18}$$

The last condition, where x_{ET} and y_{ET} are the coordinates of the impact point with respect to the centre of the electron tagger, was used to reject events in which a large amount of energy leaks over the transverse detector boundaries. The crystal calorimeters were calibrated with events having $E_{VC} \leq 0.2\,\text{GeV}$ making use of the kinematic constraint $E_{\text{ET}} + E_\gamma = E_e^0$, while the water Čerenkov counter was calibrated with those events having $E_{VC} \geq 0.2\,\text{GeV}$. In Fig. 10a) the correlation of E_γ and E_{ET} is shown for those Bremsstrahlung events with $E_{\text{VC}} \leq 0.2\,\text{GeV}$. The stability of the calibration was checked by dividing the selected event sample into 7 subsamples. For each subsample a gaussian function was iteratively fitted within $\pm 2\sigma$ to the energy sum $E_{\text{ET}} + E_\gamma$. The resulting mean values of the fits are given in Fig. 10b), separately for the two event samples with and without energy deposit in the water Čerenkov counter. For both samples the calibration could be verified within 0.5%. The relative calibration of E_γ and E_{ET} is determined with a precision of 1.3% from studies of the E_γ and E_{VC} dependence of the mean $E_\gamma + E_{\text{ET}}$. Taking into account a maximum nonlinearity of 1.3% in the response of the photon arm the global energy scale is known with a precision of 1.5% for $E_\gamma > 4\,\text{GeV}$.

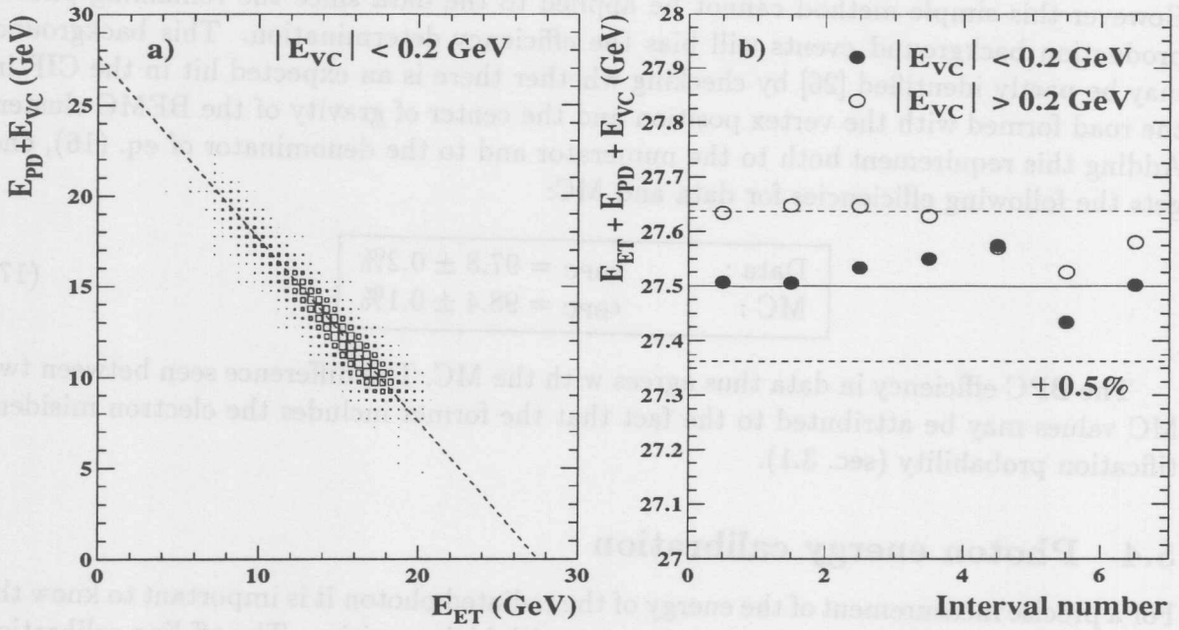

Figure 10: *Correlation of the photon and electron energy for Bremsstrahlung events in a). The energy sum is expected to be* 27.5 GeV. *In b) the mean values of the energy sum is plotted for 7 different run intervals. The calibration is stable within* $\pm 0.5\%$.

5.5 Comparison between data and MC simulation

In the previous subsections we have checked various efficiencies. Apart from the trigger efficiency, and the small difference on the vertex efficiency in the low y region, all other efficiencies were found to have been reasonably well simulated in the MC. After correcting for the trigger efficiency and the vertex efficiency, data are compared in Fig. 11 with the MC for various relevant quantities used in the reconstruction of the kinematics. The MC events generated with the GRV parametrization (F_2^{GRV}) have been reweighted by $F_2^{\mathrm{fit}}(x_{\mathrm{true}}, Q^2_{\mathrm{true}})/F_2^{\mathrm{GRV}}(x_{\mathrm{true}}, Q^2_{\mathrm{true}})$, where F_2^{fit} is a next-to-leading-order fit[6] to the measured F_2 for $Q^2 > 5\,\mathrm{GeV}^2$ based on the H1 non-radiative DIS events taken also in 1994 [6], and x_{true} and Q^2_{true} are the true kinematics at the hadronic vertex. Good agreement is observed in all cases indicating both the background estimation and the detector efficiencies are well under control.

[6]More precisely, it is the fit value only for $Q^2 > 5\,\mathrm{GeV}^2$ otherwise it is an extrapolation of the fit to lower Q^2 values.

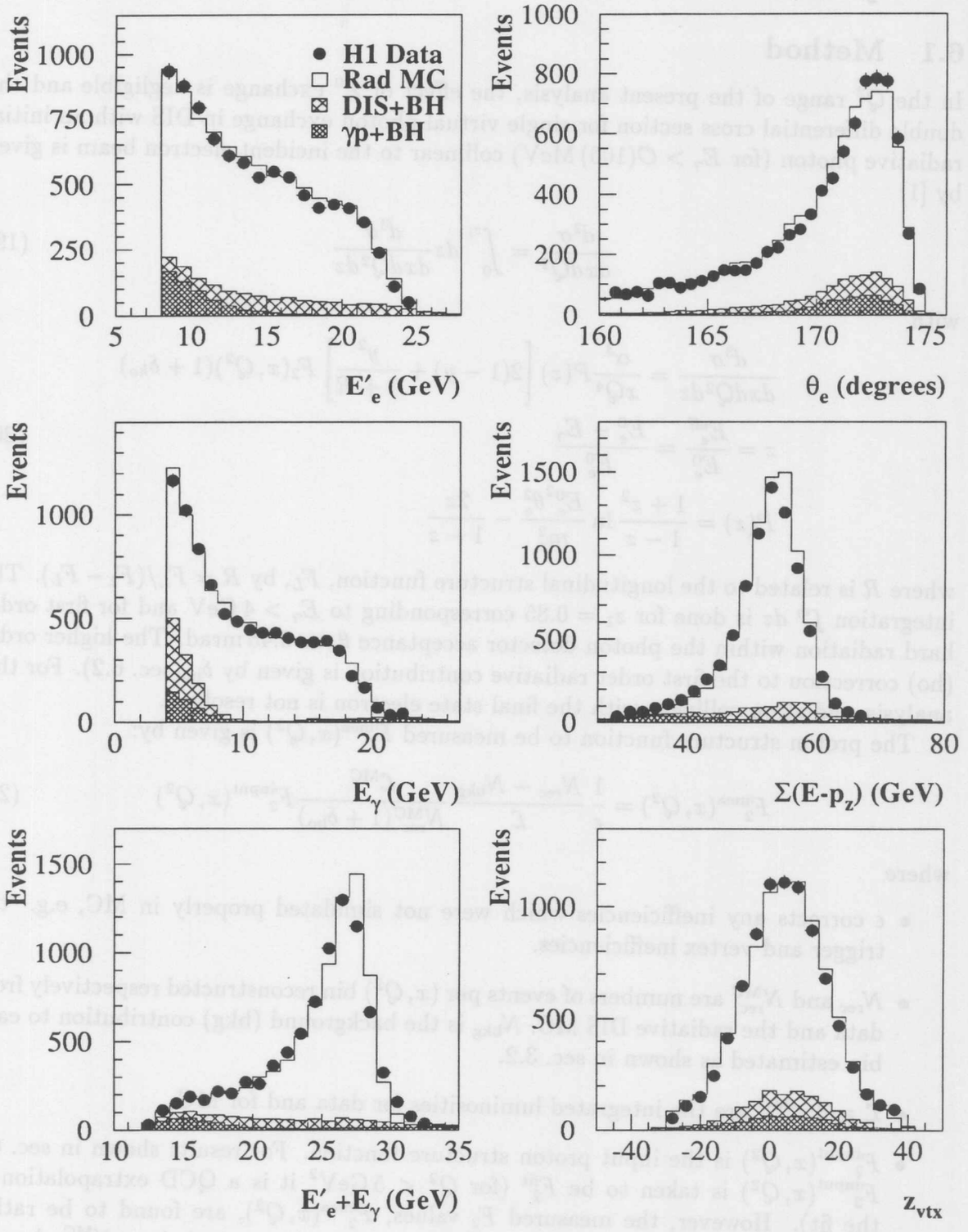

Figure 11: *A comparison between data and MC for various quantities relevant for the kinematics reconstruction.*

6 F_2 Measurement

6.1 Method

In the Q^2 range of the present analysis, the effect of Z^0 exchange is negligible and the double differential cross section for single virtual photon exchange in DIS with an initial radiative photon (for $E_\gamma > \mathcal{O}(100)\,\mathrm{MeV}$) collinear to the incident electron beam is given by [1]

$$\frac{d^2\sigma}{dxdQ^2} = \int_0^{z_1} dz \frac{d^3\sigma}{dxdQ^2dz} \tag{19}$$

with

$$\begin{aligned} \frac{d^3\sigma}{dxdQ^2dz} &= \frac{\alpha^3}{xQ^4} P(z) \left[2(1-y) + \frac{y^2}{1+R}\right] F_2(x,Q^2)(1+\delta_{ho}) \\ z &= \frac{E_e^{\mathrm{eff}}}{E_e^0} = \frac{E_e^0 - E_\gamma}{E_e^0} \\ P(z) &= \frac{1+z^2}{1-z} \ln \frac{E_e^{0\,2}\theta_a^2}{m_e^2} - \frac{2z}{1-z} \end{aligned} \tag{20}$$

where R is related to the longitudinal structure function, F_L, by $R = F_L/(F_2 - F_L)$. The integration $\int_0^{z_1} dz$ is done for $z_1 = 0.85$ corresponding to $E_\gamma > 4\,\mathrm{GeV}$ and for first order hard radiation within the photon detector acceptance $\theta_a \simeq 0.45\,\mathrm{mrad}$. The higher order (ho) correction to the first order radiative contribution is given by δ_{ho}(sec. 6.2). For this analysis, radiation collinear with the final state electron is not resolved.

The proton structure function to be measured $F_2^{\mathrm{mea}}(x,Q^2)$ is given by:

$$F_2^{\mathrm{mea}}(x,Q^2) = \frac{1}{\epsilon} \frac{N_{\mathrm{rec}} - N_{\mathrm{bkg}}}{\mathcal{L}} \frac{\mathcal{L}^{\mathrm{MC}}}{N_{\mathrm{rec}}^{\mathrm{MC}}(1+\delta_{\mathrm{ho}})} F_2^{\mathrm{input}}(x,Q^2) \tag{21}$$

where

- ϵ corrects any inefficiencies which were not simulated properly in MC, e.g. the trigger and vertex inefficiencies.
- N_{rec} and $N_{\mathrm{rec}}^{\mathrm{MC}}$ are numbers of events per (x,Q^2) bin reconstructed respectively from data and the radiative DIS MC. N_{bkg} is the background (bkg) contribution to each bin estimated as shown in sec. 3.2.
- $\mathcal{L}$ and $\mathcal{L}^{\mathrm{MC}}$ are the integrated luminosities for data and for MC.
- $F_2^{\mathrm{input}}(x,Q^2)$ is the input proton structure function. For results shown in sec. 6.3 $F_2^{\mathrm{input}}(x,Q^2)$ is taken to be F_2^{fit} (for $Q^2 < 5\,\mathrm{GeV}^2$ it is a QCD extrapolation of the fit). However, the measured F_2 values, $F_2^{\mathrm{mea}}(x,Q^2)$, are found to be rather independent of different choices of F_2^{input}, which is as expected since $N_{\mathrm{rec}}^{\mathrm{MC}}$ changes as F_2^{input} changes (eq. (21)).

6.2 Higher order QED correction

As shown in sec. 6.1, we intend to measure $F_2(x, Q^2)$ using events with collinear hard photon radiation in first order. The inclusive cross section (or number of events in each defined (x, Q^2) bin) measured in data includes higher order contributions which have to be subtracted.

The effect of high order contributions, which is dominated by multiphoton emission collinear to the incident electron, is estimated with the event generator LESKO [27]:

$$1 + \delta_{ho} = \frac{\sigma^{YFS}}{\sigma^{F}} \tag{22}$$

where σ^F and σ^{YFS} are the two options of the LESKO program. The first option includes $\mathcal{O}(\alpha)$ QED radiative corrections, and the second one describes multiphoton leptonic radiation in a framework of the Yennie-Frautschi-Suura exclusive exponentiation procedure [28]. The correction ($\delta_{\rm ho}$ in %) for the E method is shown with the upper number in each (x, Q^2) bin (separated with the dashed lines) in Fig. 12. The errors are

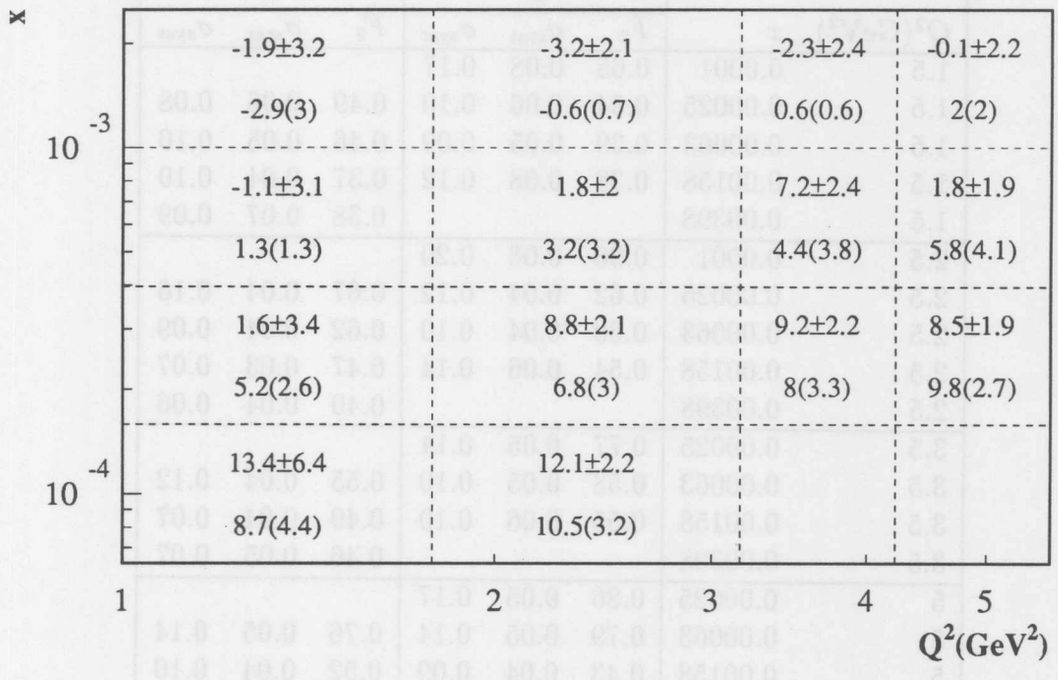

Figure 12: *Higher order QED correction $\delta_{\rm ho}$ (in %) for the E method estimated with LESKO (upper number, the error is statistical) and with an independent method based on HECTOR (lower number). The numbers in brackets are assigned systematics errors.*

statistical. The correction can be as much as 13% in the lowest x bins considered and becomes small for the high x (or low y) region. The correction has been checked with an independent method [29] in which the higher order effect was simulated using the

HECTOR package [30] with the varying incident electron beam energy $E_e^{\rm eff}$ ($= E_e^0 - E_\gamma$, E_γ being the energy spectrum of the radiated photon in first order). The results[7] are shown with the lower numbers in each bin in Fig. 12. Reasonable agreement is seen and occasional large differences are due either to an intrinsic cut on $p_T > 1\,\mathrm{GeV}$ in LESKO, which introduces some edge effect for the first Q^2 bin at $1.5\,\mathrm{GeV}^2$, or to a statistical fluctuation in LESKO, e.g. as a function of Q^2 for the x bins in the second row from the top. Since both methods give comparable results and the latter one has less fluctuation, this latter correction was used in the following with systematic uncertainties given with the numbers (in %) in brackets in Fig. 12. The correction for the Σ method is small ($\lesssim 3\%$) and is rather uniform in the (x, Q^2) bins considered.

6.3 F_2 results

The measured proton structure function F_2 values are listed in Table 2 and plotted in Fig. 13 for both kinematic reconstruction methods E and Σ. The total systematic errors

		E			Σ		
$Q^2(\mathrm{GeV}^2)$	x	F_2	$\sigma_{\rm stat}$	$\sigma_{\rm syst}$	F_2	$\sigma_{\rm stat}$	$\sigma_{\rm syst}$
1.5	0.0001	0.65	0.08	0.17			
1.5	0.00025	0.54	0.06	0.10	0.49	0.06	0.08
1.5	0.00063	0.39	0.05	0.09	0.46	0.05	0.10
1.5	0.00158	0.38	0.08	0.12	0.37	0.04	0.10
1.5	0.00398				0.38	0.07	0.09
2.5	0.0001	0.96	0.06	0.20			
2.5	0.00025	0.62	0.04	0.12	0.67	0.04	0.16
2.5	0.00063	0.60	0.04	0.10	0.62	0.04	0.09
2.5	0.00158	0.54	0.06	0.14	0.47	0.03	0.07
2.5	0.00398				0.40	0.04	0.06
3.5	0.00025	0.77	0.05	0.14			
3.5	0.00063	0.58	0.05	0.10	0.55	0.04	0.12
3.5	0.00158	0.55	0.06	0.10	0.49	0.04	0.07
3.5	0.00398				0.46	0.05	0.07
5	0.00025	0.86	0.05	0.17			
5	0.00063	0.79	0.05	0.14	0.76	0.05	0.14
5	0.00158	0.43	0.04	0.09	0.52	0.04	0.10
5	0.00398				0.46	0.04	0.09

Table 2: *Proton structure function F_2 measured with the E and Σ methods. The global luminosity uncertainty of 1.5% is not included in the quoted systematic errors.*

[7] A cut on $W^2 > 225\,\mathrm{GeV}^2$ has been applied as higher order contributions at lower W^2 values are unlikely to contribute according to Fig. 9 when a reconstructed vertex is required.

shown in Table 2 do not include the global luminosity uncertainty of 1.5%. Detailed systematic error sources are discussed in sec. 6.3.1. The results are in agreement to within the systematic errors. Since the E method has better x resolution at high y ($\gtrsim 0.15$ corresponding to low x values) region, F_2 points from this method are taken with those from the Σ method in the low y region such that the measurable kinematic domain is significantly extended.

6.3.1 Systematic studies

Many sources of systematic error have been considered. Most of them are common to the E and Σ methods, while others are only specific to one or the other. These sources include:

- The uncertainty due to the background subtraction: 4% for the DIS+BH type and 30% for the γp+BH type as described in sec. 3.2.
- The uncertainty on the electron energy scale: 1% [9] for electrons measured in the BEMC.
- The uncertainty on the hadronic energy scale: 4% is assigned to take into account both the energy calibration uncertainty and the noise treatment uncertainty in the various parts of the LAr detector.
- A shift of up to 1 mrad for polar angle measurement of scattered electrons.
- The uncertainty on the photon energy scale: 1.5% as shown in sec. 5.4. The photon energy resolution in radiative MC was found to be slightly too good when compared with that in data and therefore an additional smearing of $4\%/\sqrt{E_\gamma}$ has been added to the MC events.
- The uncertainty of the selection has been taken into account by varying various selection cuts:

$$
\begin{aligned}
& E_e > 8\,\mathrm{GeV} \rightarrow 8.5\,\mathrm{GeV}\,, \\
& E_\gamma > 4\,\mathrm{GeV} \rightarrow 4.5\,\mathrm{GeV}\,, \\
& RCLU < 5\,\mathrm{cm} \rightarrow 4\,\mathrm{cm}\,, \\
& DBPC < 4\,\mathrm{cm} \rightarrow 3.8\,\mathrm{cm}\,, \\
& |z_{\mathrm{vtx}} - z_0| < 35\,\mathrm{cm} \rightarrow 30\,\mathrm{cm} \\
& \sqrt{x^2_{\mathrm{BPC}} + y^2_{\mathrm{BPC}}} > 15\,\mathrm{cm} \rightarrow 15.5\,\mathrm{cm}\,, \\
& |x_{\mathrm{BPC}}| + |y_{\mathrm{BPC}}| > 18\,\mathrm{cm} \rightarrow 18.5\,\mathrm{cm}\,, \\
& \Delta < 0.5 \rightarrow 0.3\,.
\end{aligned}
\tag{23}
$$

  The effect on F_2 was typically 5% but could reach up to 10% for some edge bins. The photon detector acceptance was checked with an independent MC (LESKO) and an uncertainty of 2% was added to the acceptance uncertainty.

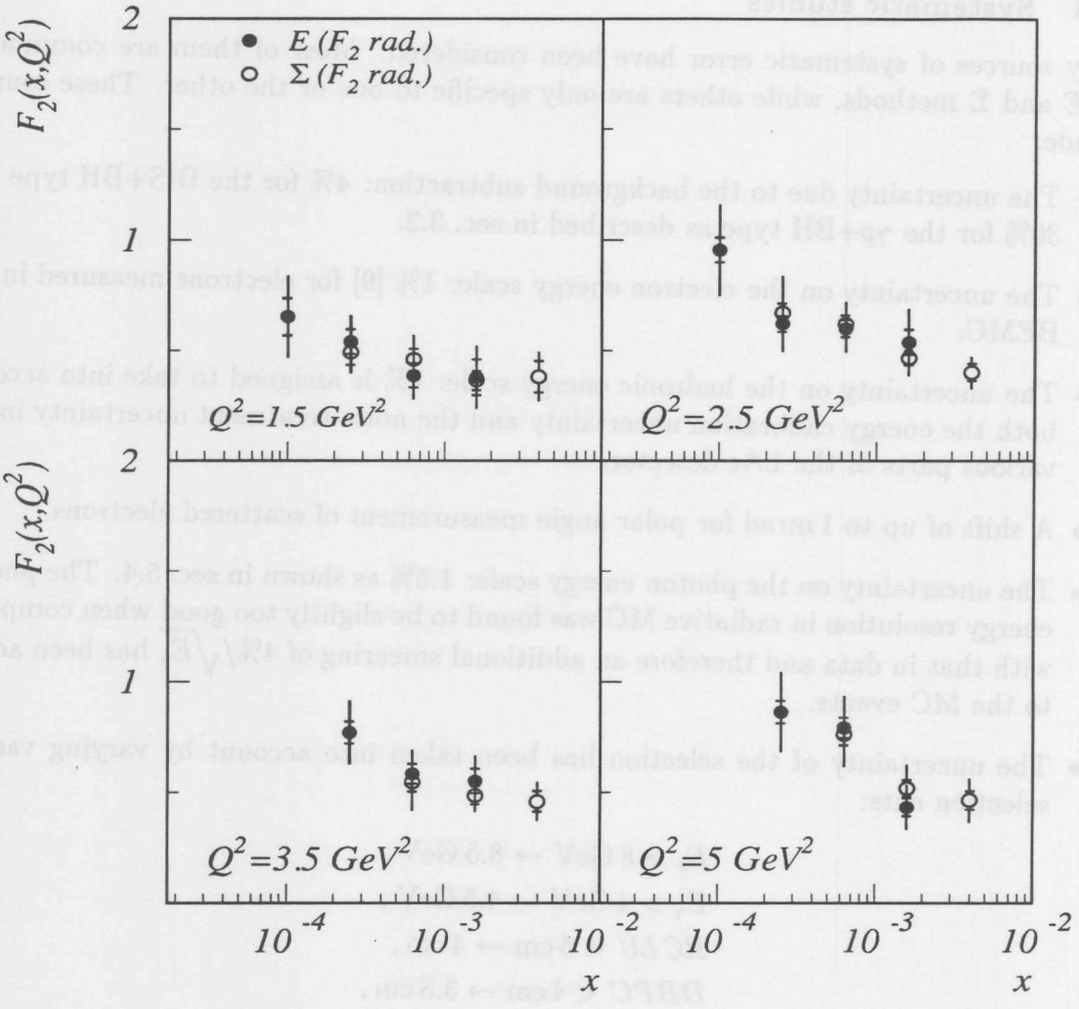

Figure 13: *A comparison of measured $F_2(x, Q^2)$ values using the E and the Σ methods. The inner error bars show the statistical errors only, while the outer ones represent statistical and systematic errors added in quadrature.*

- Electron misidentification ($\sim 3\%$) leads to wrong reconstruction of the event kinematics. The uncertainty on F_2 is estimated by replacing the fake electron by the true one in the MC.
- The higher order QED radiation correction uncertainty as shown in sec. 6.2.
- The vertex efficiency was checked with the CIP method as explained in sec. 5.2. The uncertainty varies between 10% at high x and 4% at small x for the Σ method (10% for the E method).
- The BPC efficiency uncertainty: an agreement to within 1% between data and MC after the residual γp in the data had been rejected using the CIP electron validation method.
- The trigger efficiency uncertainty: the strategy taken in this analysis required presence of the rather efficient subtrigger bit s_0 and corrected for its inefficiency determined with sufficient precision using independent data selected with tracker related triggers. Since the trigger for DIS events is rather redundant, one may assume that the data sample has no event loss if no specific trigger is required. Both approaches have been implemented, and the difference on F_2 was quoted as the uncertainty of the trigger correction.
- The structure function uncertainty was taken into account by looking at the difference in F_2 by either taking directly the structure function (GRV) used in the radiative DIS MC event generation as F_2^{input} or a different input F_2^{fit} (for $Q^2 < 5\,\text{GeV}^2$ it is a QCD extrapolation to low Q^2 of the fit) and having $N_{\text{rec}}^{\text{MC}}$ reweighted by $F_2^{\text{fit}}/F_2^{\text{GRV}}$.
- The uncertainty due to the unknown function R: the extraction of F_2 from the measured cross section depends on the input R. The difference on F_2 between two extreme values $R = 0$ and $R = \infty$ was quoted as the systematic error.
- The radiative MC has about twice the statistics of the real data; therefore the MC statistical uncertainty is not negligible and has been included as one of the systematic uncertainties on F_2.

6.3.2 Cross check

To ensure that all detector effects and the analysis chain are correctly treated an independent analysis has been performed. The main differences between the two analyses are:

- Only events from the period where HERA was running with positrons were accepted. The relevant subdetectors had to be switched on for more than 80% of the time for each accepted run. These requirements lead to a reduction of the integrated luminosity to $\int \mathcal{L} = 2.4\,\text{pb}^{-1}$.

- The radius of the electromagnetic cluster: $RCLU < 4\,\mathrm{cm}$ (cf. 5 cm in eq. (1)).
- BH events used for simulating the background pile-up events were selected directly from data while they were generated events in the other analysis (sec. 3.3).
- The kinematics calculated with the Σ method was based on clusters while it was based on cells in the other analysis.

In Fig. 14 the values obtained by this independent analysis, labeled as "Analysis 2", are shown and compared to the values shown in Fig. 13, labeled as "Analysis 1". Agreement within the statistical error is found for most of the points and differences are mainly observed at very low x values, for instance the first E and Σ point at $1.5\,\mathrm{GeV}^2$, which correspond to low energy and large angle scattered electrons. Thus larger systematic effects are expected at these points (Table 2)[8].

6.3.3 Discussions

The final F_2 values are compared in Fig. 15 with those from other measurements and with F_2 parametrizations. Several observations are in order:

- This measurement has allowed to extend the HERA F_2 measurement for Q^2 down to $1.5\,\mathrm{GeV}^2$.
- The measurement is in good agreement in the common x region with other measurements from both H1 (based on non-radiative DIS events) [6] and ZEUS [7] and from fixed target experiments [31, 32] at high x.
- This measurement has allowed to fill the gap between the HERA measurements at low x and that of fixed target experiments at high x.
- All measurements are compatible with the GRV [19] calculation except in the very low x region where the measurements seem to be (systematically) below the prediction.
- The parametrization DOLA [33], which is motivated by Regge theory and relates the structure function to Reggeon exchange phenomena, seems to undershoot the data in all shown bins even at $Q^2 = 1.5\,\mathrm{GeV}^2$.
- The measurement agrees well with an extrapolation of a next-to-leading-order QCD fit [6] to the H1 data for $Q^2 \geq 5\,\mathrm{GeV}^2$.

[8]This first electron point was therefore not included in [6].

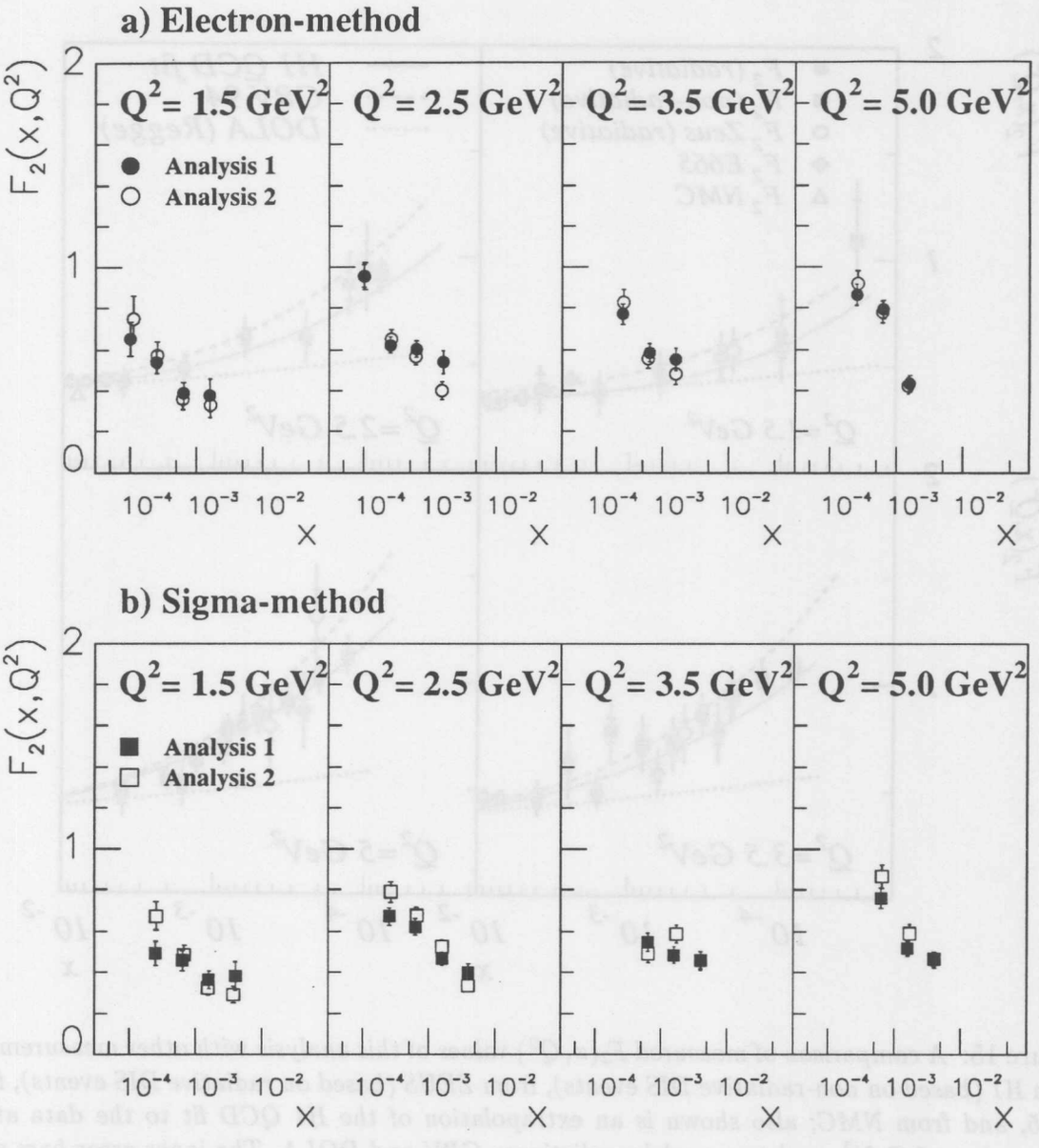

Figure 14: *Comparison of the proton structure function $F_2(x, Q^2)$ obtained by two independent analyses. The errors shown are statistical only.*

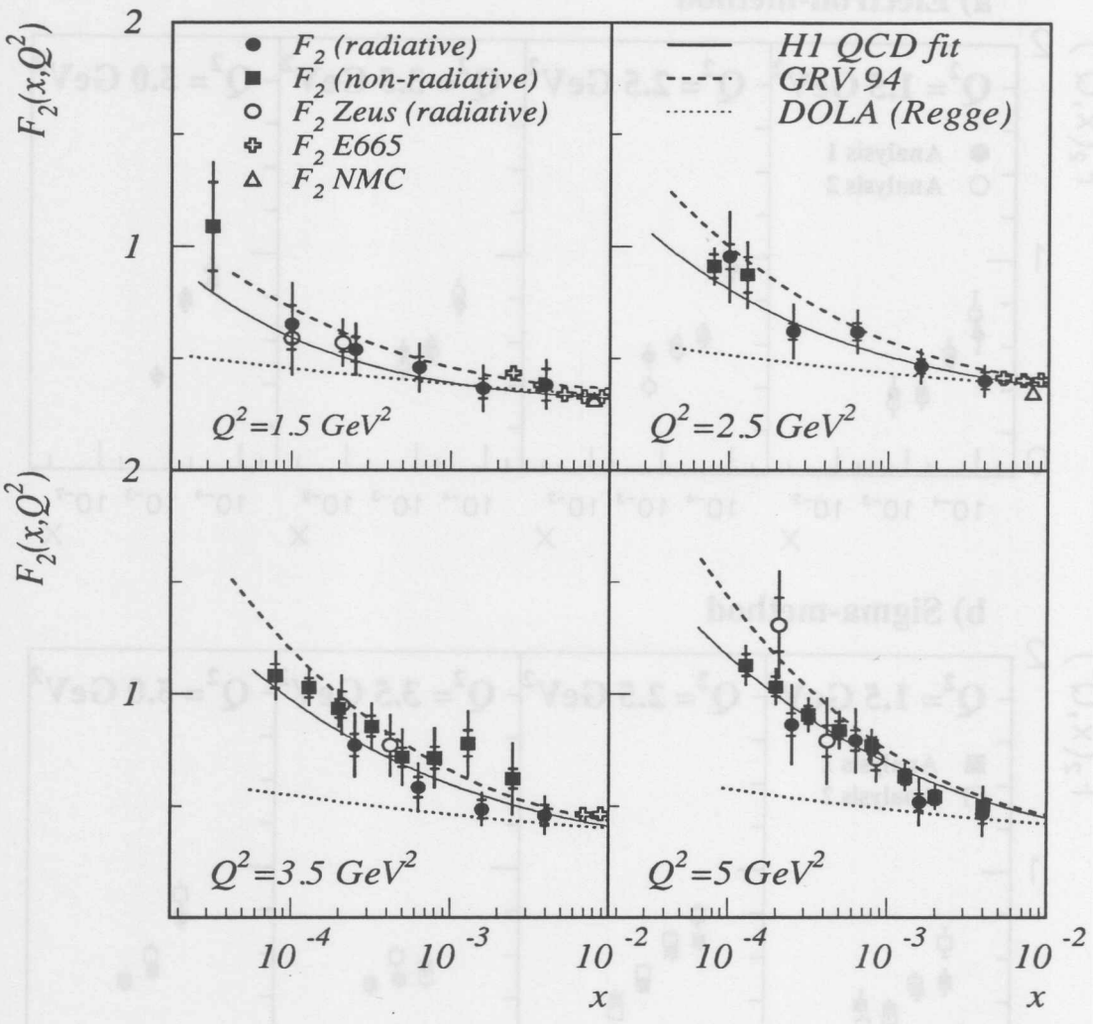

Figure 15: *A comparison of measured $F_2(x, Q^2)$ values of this analysis with other measurements from H1 (based on non-radiative DIS events), from ZEUS (based on radiative DIS events), from E665, and from NMC; also shown is an extrapolation of the H1 QCD fit to the data at Q^2 values above 5 GeV^2, and two model predictions: GRV and DOLA. The inner error bars show the statistical errors only, while the outer ones represent statistical and systematic errors added in quadrature.*

6.3.4 A phenomenological fit to the data

The x dependence at fixed Q^2 of F_2 may be fitted[9] with a single parameter λ as:

$$F_2 \propto x^{-\lambda} \tag{24}$$

$$\sim W^{2\lambda}. \tag{25}$$

The second equation holds for small x and follows because x is connected with W^2, the invariant mass squared of the hadronic system (after neglecting the proton mass term):

$$W^2 = Q^2 \left(\frac{1}{x} - 1\right). \tag{26}$$

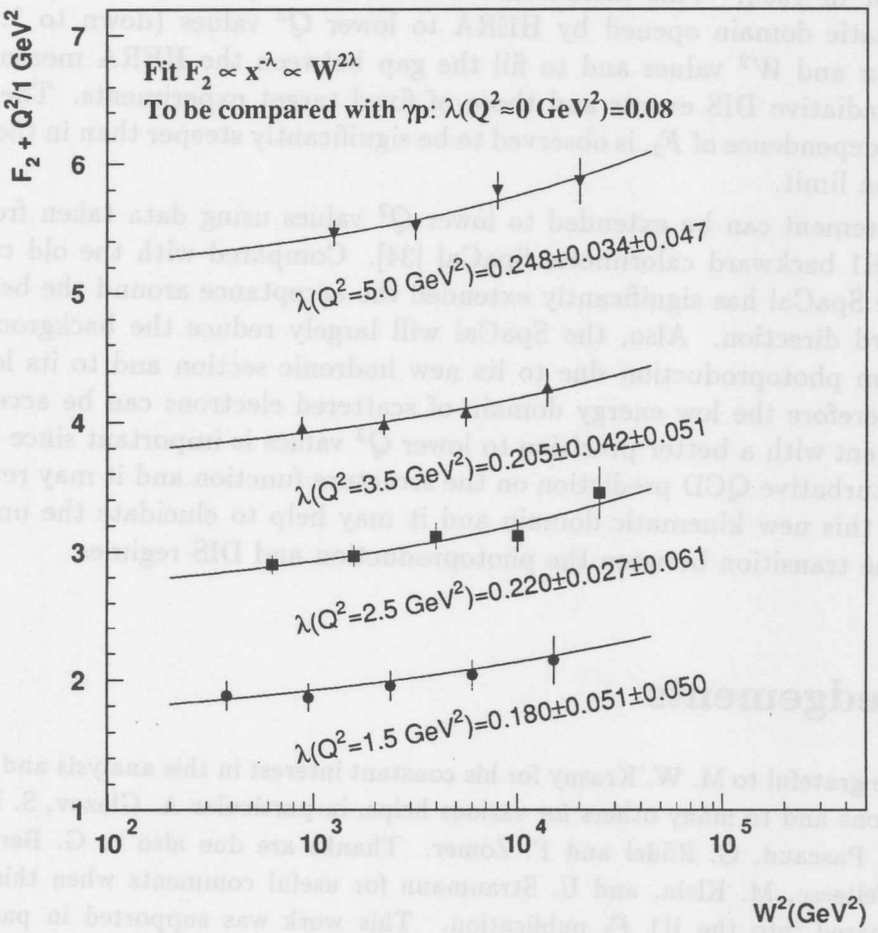

Figure 16: *A fit to the measured F_2 as a function of W^2. The first errors on λ are statistical and the second ones systematic. The error bars represent statistical and systematic errors added in quadrature.*

[9]Here only F_2 values from this analysis have been used in the fit, which is different from [6] where F_2 values from other analysis based on non-radiative events are also included.

The dependence of F_2 as a function of W^2 is shown in Fig. 16 together with the fitted λ values. There is no evidence for any variation[10] of λ with Q^2 in the range $1.5 \leq Q^2 \leq 5\,\mathrm{GeV}^2$. When compared with measurements at $Q^2 \simeq 0$, namely of the total photoproduction cross section, there is evidence for a significantly steeper dependence on W^2 at these moderate values of Q^2.

7 Summary and outlook

The proton structure function $F_2(x, Q^2)$ has been measured using radiative DIS events with hard real photon emission collinear to the incident electron from data taken with the H1 detector in 1994. This measurement has made it possible to extend further the new kinematic domain opened by HERA to lower Q^2 values (down to $1.5\,\mathrm{GeV}^2$) at comparable x and W^2 values and to fill the gap between the HERA measurements based on non-radiative DIS events and those of fixed target experiments. The W^2, or equivalently x, dependence of F_2, is observed to be significantly steeper than in the $Q^2 \simeq 0$ photoproduction limit.

This measurement can be extended to lower Q^2 values using data taken from 1995 with the new H1 backward calorimeter SpaCal [34]. Compared with the old calorimeter BEMC, the SpaCal has significantly extended the acceptance around the beam pipe in the backward direction. Also, the SpaCal will largely reduce the background contamination from photoproduction due to its new hadronic section and to its low noise behaviour. Therefore the low energy domain of scattered electrons can be accessed. A new measurement with a better precision to lower Q^2 values is important since it allows to test the perturbative QCD prediction on the structure function and it may reveal new phenomena in this new kinematic domain and it may help to elucidate the underlying dynamics of the transition between the photoproduction and DIS regimes.

Acknowledgements

The authors are grateful to M. W. Krasny for his constant interest in this analysis and for many helpful discussions and to many others for various helps, in particular A. Glazov, S. Levonian, A. Panitch, C. Pascaud, G. Rädel and F. Zomer. Thanks are due also to G. Bernardi, A. de Roeck, J. Feltesse, M. Klein, and U. Straumann for useful comments when this analysis was being prepared into the H1 F_2 publication. This work was supported in part by the Bundesministerium für Bildung, Wissenschaft, Forschung und Technologie, Germany (grant-no: 6DO57I) and by the Graduiertenkolleg für Elementarteilchenphysik at the University of Dortmund.

[10] However, a clear variation of λ with Q^2 shows up when these λ values are shown together with those from higher Q^2 (cf. Fig. 8 in [6]).

References

[1] M.W. Krasny et al., Z. Phys. C53 (1992) 687.

[2] M. Fleischer, PhD thesis, Universität Hamburg, 1994.

[3] H1 Collab., T. Ahmed et al., Z. Phys. C66 (1995) 529

[4] U. Obrock, PhD thesis, Universität Dortmund, 1994.

[5] L. Favart, PhD thesis, Université Libre de Bruxelles, 1995.

[6] H1 Collab., S. Aid et al., "A Measurement and QCD Analysis of the Proton Structure Function $F_2(x, Q^2)$ at HERA", DESY 96-39 (1996), submitted to Nucl. Phys.

[7] ZEUS Collab., M. Derrick et al., DESY 95-193, to appear in Z. Phys. C

[8] H1 Collab., I. Abt et al., "The H1 detector at HERA", DESY H1-96-01 (1996).

[9] J. Bán et al., Nucl. Instr. and Meth. A 372 (1996) 399 - 414.

[10] H. Bethe and W. Heitler, Proc. Roy. Soc. **A146** (1934) 83.

[11] F. Jacquet and A. Blondel, Proceedings of the "Study for an *ep* Facility in Europe" (1979) 391.

[12] S. Levonian, private communication, and
N. Gogitidze and S. Levonian, H1 internal note, H1-02/96-471 (1996).

[13] R. Brun et al., GEANT3 User's Guide, CERN DD/EE/84-1 (1987).

[14] G. A. Schuler and H. Spiesberger, Proceedings of the Workshop Physics at HERA, Vol. 3, eds. W. Buchmüller and G. Ingelman, DESY (1992) p. 1419.

[15] A. Kwiatkowski, H. Spiesberger and H.-J. Möhring. Comp. Phys. Comm. 69 (1992) 155.

[16] G. Ingelman, Proceedings of the Workshop Physics at HERA, Vol. 3, eds. W. Buchmüller and G. Ingelman, DESY (1992) p. 1366.

[17] L. Lönnblad, Comp. Phys. Comm. 71 (1992) 15.

[18] T. Sjöstrand and M. Bergtsson, Comp. Phys. Comm. 43 (1987) 367.

[19] M. Glück, E. Reya and A. Vogt, Z. Phys. C53 (1992) 127; Phys. Lett. B306 (1993) 391.

[20] H1 Collab., T. Ahmed et al., Nucl. Phys. B439 (1995) 471.

[21] ZEUS Collab., M. Derrick et al., Z. Phys. C65 (1995) 379.

[22] R. Engel, Proceedings of the XXIXth Rencontre the Moriond, ed, J. Tran Thanh Van, (edition Frontieres, 1994) 231.

[23] U. Bassler and G. Bernardi, Nucl. Instr. Meth. A361 (1995) 197.

[24] S. Bentvelsen et al., Proceedings of the Workshop Physics at HERA, Vol.1, ed. W. Buchmüller and G. Ingelmann, DESY (1992) p.23; C. Hoeger, ibid, p.43

[25] A. Panitch and P. Marage, "Vertex reconstruction using BPC and CIP in DIS", H1 internal note H1-05/93-297.

[26] P. Marage, A. Panitch, and F. Zomer, "F_2 Measurement at x-values around 10^{-4} using the Satellite Bunch", H1 internal Note H1-07/94-369.

[27] S. Jadach and W. Płazek, Proceedings of the Workshop on Physics at HERA, Vol. 3, (1991) p.1330; W. Płazek, PhD thesis, Acta Physica Polonica **B24** (1993) 1229.

[28] D. R. Yennie, S. C. Frautschi, and H. Suura, Ann. Phys. (NY) **13** (1961) 379.

[29] A. Glazov, Private comunication.

[30] A. Arbuzov et al., "HECTOR 1.00 A Program for the calculation of QED, QCD and electroweak corrections to ep and lN deep inelastic neutral and charged current scattering", DESY 95-185.

[31] E665 Collab. e.g. A. V. Kotwal, "Proton and Deuteron Structure Functions in Muon Scattering at 470 GeV", to be published in Proceedings of the XXXth Rencontres de Moriond, QCD and High Energy Interactions, Les Arcs, France, March 19-26, 1995, FERMILAB-Conf-95/046-E (1995).

[32] NMC Collab., M. Arneodo et al., Phys. Lett. **B364** (1995) 107.

[33] A. Donnachie and P. V. Landshoff, Z.Phys. **C61** (1994) 139.

[34] H1 SPACAL Group, T. Nicholls et al., "Performance of an Electromagnetic Lead/Scintillating-Fibre Calorimeter for the H1 Detector", DESY 95-165 (1995); R.-D. Appuhn et al., "Hadronic Response and e/π Separation with the H1 Lead/Fibre Calorimeter", DESY 95-250 (1995).